

SU(3) flavor symmetry considerations for the $\bar{K}N$ coupled channels system

P. C. Bruns, A. Cieplý*

Nuclear Physics Institute of the Czech Academy of Sciences, 250 68 Řež, Czechia

Abstract

We study the impact of SU(3) flavor symmetry breaking on the properties of dynamically generated Λ^* states within an effective separable potential model describing the coupled channels $\bar{K}N$ system. The model is based on the chiral meson-baryon Lagrangian at next-to-leading order, and constitutes an improvement over a previous model developed by our group, with its applicability being extended to higher energies covering the $\Lambda(1670)$ resonance region. It is demonstrated that the ratios of channel couplings to the resonant states can vary dramatically when the flavor breaking is gradually switched off, tracing a path to the restored SU(3) symmetry. We conclude that the couplings determined from physical observables cannot be used to reliably relate a given resonance to a specific flavor multiplet.

Keywords: $\bar{K}N$ interactions, SU(3) flavor symmetry, Λ^* resonances

1. Introduction

In the limit of exact SU(3) flavor symmetry ($m_u = m_d = m_s$), and when only the strong interaction is relevant, all hadrons can be classified according to the flavor multiplet they belong to [1]. Considering the real world, where flavor symmetry is broken, it appears that this classification is still very useful for a basic understanding of the structure of hadrons, even though it is only an approximate one. In a framework employing chiral effective Lagrangians [2, 3, 4, 5, 6] (as well as in Lattice QCD), one can

*Corresponding author

Email address: cieply@ujf.cas.cz (A. Cieplý)

even tune the flavor breaking terms away from their physical values, and establish a connection to a hypothetical flavor-symmetric world, where the flavor classification strictly applies. In the present work, we study the impact of such a procedure on Λ^* resonances (isoscalar baryons with strangeness $S = -1$) that are dynamically generated in a coupled-channel framework based on effective potentials derived from a chiral Lagrangian [7, 8, 9, 10, 11]. An earlier study in this direction can be found in Sec. 3 of Ref. [11], where only a leading order (LO) Weinberg-Tomozawa (WT) interaction kernel was employed. There, an $SU(3)$ flavor singlet and two degenerate octet states were generated in the flavor-symmetric limit. Here we aim at extending such an analysis by the inclusion of Born and next-to-leading-order (NLO) contact terms in the interaction kernel, which are indispensable to obtain a satisfying description of the data from the kaon-nucleon threshold up to the region of the $\Lambda(1670)$ resonance.

The early analyses [7, 8] based on chirally motivated coupled-channels $\bar{K}N$ interactions concentrated on reproducing the K^-p total cross sections at low kaon momenta and the threshold branching ratios, fitting the model parameters to relatively old bubble chamber data. The later measurements of kaonic hydrogen characteristics by the DEAR [12] and SIDDHARTA [13] collaborations put more stringent constraints on the theoretical models, though the focus remained on the energy region dominated by the $\Lambda(1405)$ resonance [14, 15]. This is also the case with the Prague model [16], which we use as a guideline for our current analysis and for testing the model dependence of the presented results. The particular model used in our study is based on the same framework we adopted for treating the $\eta N - \eta' N$ interactions and aims at covering a broader energy region, from the $\bar{K}N$ threshold up to the $\Lambda(1670)$ domain. This also follows a recent trend of extending the available chirally motivated $\bar{K}N$ models to energies much higher than those dominated by the $\Lambda(1405)$, see e.g. [17, 18, 19].

A novel feature of the present work lies in an emphasis on the behavior of ratios of couplings of the resonances to various meson-baryon (MB) states. These ratios are tightly constrained in the fully flavor-symmetric case, and we assess the applicability of the $SU(3)$ -relations in the presence of realistic flavor-symmetry breaking. To achieve this task we utilize a new coupled-channel $\bar{K}N$ model described in some detail in Sec. 2. In Sec. 3, we discuss the $SU(3)$ symmetry constraints on the resonance couplings. There, we restrict ourselves to some symmetry relations that will be needed for the discussion of our results in Sec. 4. Then, we present the outcome of our updated fits, and

discuss the behavior of the resulting resonance pole positions and couplings when the flavor-breaking is continuously switched off. This allows us to relate our dynamically generated resonances to pertinent flavor multiplets. The conclusions we draw from our findings are provided in Sec. 5.

2. Coupled channels $\bar{K}N$ model description

The notation and conventions follow closely those detailed in our previous work on the $\eta N - \eta' N$ coupled channels system [20]. Here we just disregard the $\eta - \eta'$ mixing, assuming the η meson involved in channels coupled to the $\bar{K}N$ system is represented by a pure octet state. The tree-level contributions derived from a manifestly Lorentz invariant chiral Lagrangian are written in a form

$$v_{0+}(s) = \frac{\sqrt{E+m}}{F_\Phi} \left(\frac{C(s)}{8\pi\sqrt{s}} \right) \frac{\sqrt{E+m}}{F_\Phi} \quad (1)$$

where we employ a convenient channel-matrix notation. The diagonal matrices E , m and F_Φ are assembled from the baryon center-of-mass (c.m.) energies, baryon masses and meson decay constants of the respective channels. The channel matrix $C(s)$ contains all the details specific to the effective vertices and the various elastic and inelastic MB reactions. In some more detail,

$$\begin{aligned} C(s) &= \frac{1}{4} \{(\sqrt{s}-m), C^{WT}\} - C^{NLO}(s) \\ &\quad - \frac{(\sqrt{s}-m)C^{BD}(\sqrt{s}-m)}{\sqrt{s}+m_c} - C^{BC}(s), \\ C^{NLO}(s) &= 2M_\pi^2 C^\pi + 2M_K^2 C^K - 2q^0(s) C^d q^0(s). \end{aligned} \quad (2)$$

The q^0 represents the diagonal channel matrix $q^0(s) = (s - m^2 + M^2)/(2\sqrt{s})$, featuring the meson c.m. energies in the respective MB channels, while s is the usual Mandelstam variable given by the square of the two-body c.m. energy and M is the meson mass matrix. The channel matrices C^{WT} , $C^{NLO}(s)$, C^{BD} and $C^{BC}(s)$ contain the couplings derived from the WT term, the contact NLO terms, and the Born direct and crossed terms, respectively. Their exact form appropriate for the $\bar{K}N$ system can be found e.g. in [21]. We also note that when dealing with the crossed Born term $C^{BC}(s)$ we adopt the prescription provided in Appendix D in [20] but keep only the term linear in energy, omitting the last quadratic contribution given in Eq. (D.10)

there. This approximation was introduced to tame unphysical divergences at subthreshold energies appearing when an exact BC-term contribution is projected onto the s-wave. We checked that the approximated formula works quite well and reproduces the exact form in a broad interval of energies.

Following Refs. [16] and [20] the s-wave scattering amplitude for isospins $I = 0$ and $I = 1$ is obtained as an algebraic solution of the Lippmann-Schwinger equation with the interaction kernel constructed from the tree-level amplitudes, Eq. (1), by sandwiching them with the Yamaguchi form-factors

$$g_{jb}(p) = \left(1 + p^2/\alpha_{jb}^2\right)^{-1}, \quad (3)$$

that introduce channel dependent inverse ranges α_{jb} , where p stands for the modulus of the momentum of meson j in the c.m. frame. At the same time, the parameters α_{jb} serve as soft cutoffs to regularize the MB loop functions $G(s)$. The scattering amplitude is then obtained in a separable form

$$f_{0+}^I(s) = g(s) [1 - v_{0+}^I(s) G(s)]^{-1} v_{0+}^I(s) g(s). \quad (4)$$

Here $g(s)$ is the Yamaguchi form factor with p replaced by $q(s)$, the modulus of the on-shell MB c.m. three-momentum in the respective channel. The diagonal matrix $G(s)$ is composed from MB loop functions and can be evaluated analytically, see Eq. (8) in [20]. One can easily check that f_{0+}^I satisfies partial-wave unitarity in the considered two-body channels space.

The low energy constants (LECs) that provide couplings for the terms included in the chiral Lagrangian and the inverse ranges introduced to regularize the loop function integrals need to be determined in fits to experimental data. When dealing with $\bar{K}N$ interactions at low energies one standardly includes the experimental data on total cross sections for reactions going from the initial K^-p state to all channels that are open at the threshold (or slightly above it in case of \bar{K}^0n) [22, 23, 24, 25, 26, 27]. These are complemented by the data on three threshold branching ratios γ , R_c and R_n [28, 29], and on the measurement of the characteristics of the kaonic hydrogen atom, the 1s level energy shift $\Delta E_N(1s)$ and absorption width $\Gamma(1s)$ caused by strong interaction [13]. As we aim at performing a more complete analysis of dynamically generated Λ^* resonances, it is desirable to reproduce well not only the $\Lambda(1405)$ but cover the energies where the $\Lambda(1670)$ resonance manifests itself too. For this reason we also include in our fits the data on the total cross sections for reactions that go to the $\eta\Lambda$ and $\eta\Sigma$ channels [30, 31, 32]. Since our $\bar{K}N$ model contains a relatively large number of parameters, it

is essential to fix some of them to already established values. By doing so we reduce the number of degrees of freedom which in turn provides a better control over the fitting procedure. First of all it seems natural to adopt the following:

- Meson decay constants $F_\pi = 92.3$ MeV, $F_K = 1.193 \cdot F_\pi = 110.1$ MeV, $F_\eta = 1.28 \cdot F_\pi = 118.3$ MeV complying with the PDG [33] and the lattice results [34].
- The MB axial couplings $F = 0.46$ and $D = 0.80$ as extracted in analyses of hyperon decays [35].
- $b_D = 0.1$ GeV⁻¹, about the average value from various fits and estimates available in the literature. The b_0 and b_F are left to be determined in the fits as they appear less stable due to renormalization caused by loop function contributions [20].

This setting leaves us with 12 parameters to be determined in the fits: 6 inverse ranges α_{jb} , 4 d -couplings, b_0 and b_F .

The fit was performed using the MINUIT routine from the CERNLIB library to minimize the χ^2 per degree of freedom defined as

$$\chi^2/dof = \frac{\sum_i N_i}{N_{obs}(\sum_i N_i - N_{par})} \sum_i \frac{\chi_i^2}{N_i} \quad (5)$$

where N_{par} is the number of fitted parameters, N_{obs} is a number of observables, N_i is the number of data points for an i -th observable, and χ_i^2 stands for the total χ^2 computed for the observable. Eq. (5) guarantees an equal weight of the fitted data from various processes (i.e. for different observables). We have achieved $\chi^2/dof = 1.31$, and the fitted parameters are provided in Table 1 aside the values adopted in a previous Prague fit tagged as the NLO30 model in [16]. In the latter, the fitting procedure was different and only 7 parameters were fitted to the data that did not include the cross sections to the $\eta\Lambda$ and $\eta\Sigma$ channels that open at higher energies. Considering the differences between the current and NLO30 model fit procedures it is not surprising that the two parameter sets differ significantly with respect to some parameter values. In particular it looks that the inverse ranges α_{jb} for channels opening at higher energies were underestimated in the NLO30 model.

Table 1: The inverse ranges (in MeV) and NLO couplings (in GeV^{-1}) obtained in fits of low energy K^-p data. The parameters used by the previous NLO30 Prague model [16] are shown for comparison too. The values marked with an asterisk were kept fixed in the respective fits.

parameter	current fit	NLO30 fit
$\alpha_{\pi\Lambda}$	400.0	297.0
$\alpha_{\pi\Sigma}$	509.2	490.6
$\alpha_{\bar{K}N}$	752.0	699.7
$\alpha_{\eta\Lambda}$	979.7	700.0*
$\alpha_{\eta\Sigma}$	797.2	700.0*
$\alpha_{K\Xi}$	1078.5	700.0*
d_1	-0.119	-0.368
d_2	0.074	0.048
d_3	0.096	0.088
d_4	0.556	-0.358
b_0	0.525	-0.321*
b_D	0.100*	0.064*
b_F	-0.077	-0.209*

Our reproduction of the fitted cross sections (as a function of the MB c.m. energy $W = \sqrt{s}$) is shown in Figure 1 in comparison with the predictions of the Prague NLO30 model [16]. As the experimental data come from relatively old bubble chamber measurements, they are not very precise and the $\bar{K}N$ models have no problem to reproduce them. Though, we note that the NLO30 model is missing completely with regards to the $\eta\Lambda$ and $\eta\Sigma$ cross sections that were not included in the respective fit. There, our current model does really well when reproducing the $\Lambda(1670)$ structure observed above the channel threshold in the $\eta\Lambda$ cross section.

The branching ratios measured at the $\bar{K}N$ threshold and the kaonic hydrogen characteristics put much tighter restrictions on the theoretical models. In Table 2 we show how these data are reproduced by the current and the NLO30 models. The same table also presents the model predictions for the poles of the scattering amplitude generated in the $I = 0$ sector. The z_1 and z_2 poles are found on the $[-, +, +, +]$ Riemann sheet (RS) and are both assigned to the $\Lambda(1405)$ resonance. The z_3 pole appears on the $[-, -, -, +]$

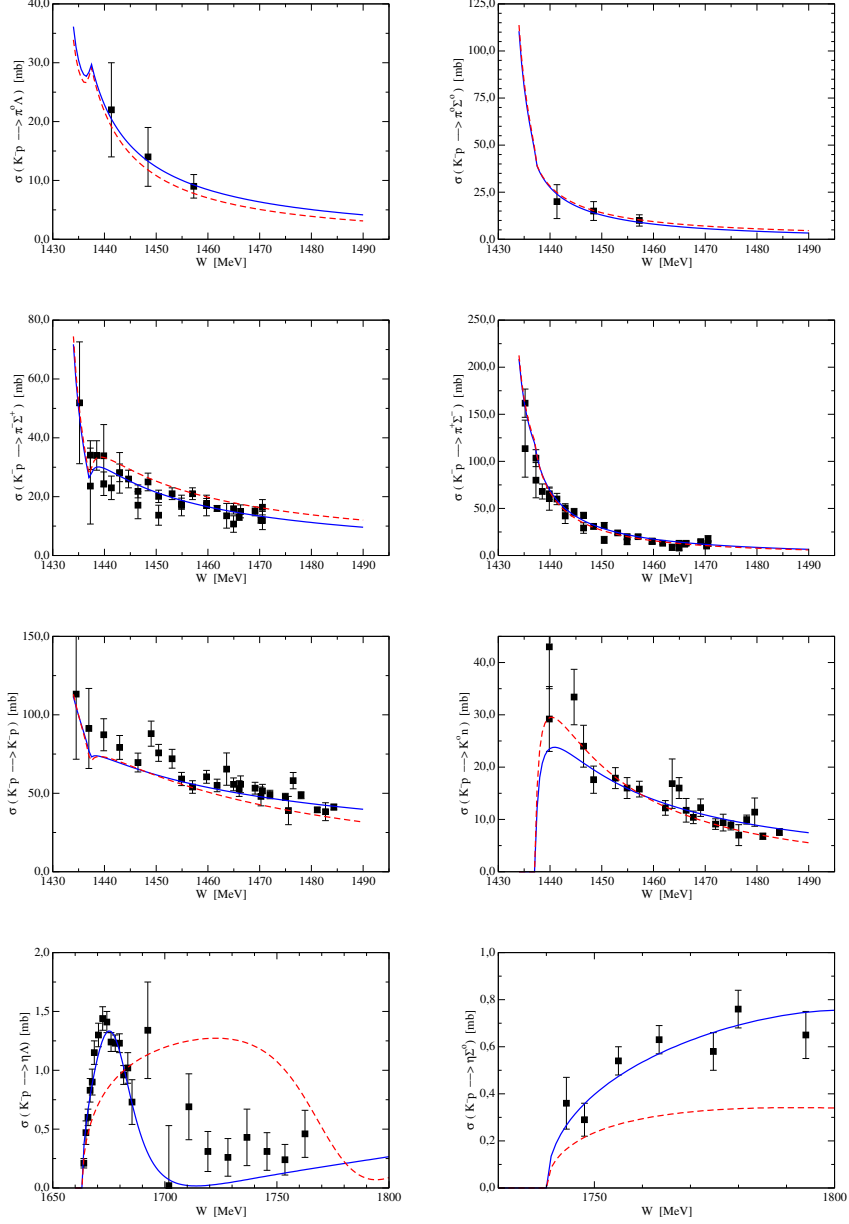


Figure 1: The $K^-p \rightarrow MB$ total cross sections. Continuous blue lines show our current model predictions, the dashed red lines the predictions of the NLO30 Prague model.

RS and is related to the $\Lambda(1670)$ resonance. As we already mentioned the NLO30 model did not include the cross sections data available at the higher energies, so it is not surprising that its prediction of the $\Lambda(1670)$ pole position is completely off the mark. However, it is worth noting that even in this case a third isoscalar pole is still predicted by the chirally motivated coupled channels model, and inclusion of relevant experimental data brings the pole position in a good agreement with the PDG accounts on the $\Lambda(1670)$. Thus, we conclude that both discussed models predict three dynamically generated Λ^* states, a feature which is completely in line with results provided by other $\bar{K}N$ approaches based on chiral Lagrangians. The two-pole structure of $\Lambda(1405)$ is a typical feature of coupled-channel models based on chiral symmetry [36, 37, 38, 39].

Table 2: Fitted branching ratios and characteristics of kaonic hydrogen in comparison with the experimental data. The positions and assignment of dynamically generated Λ^* resonances are shown as well.

	current fit	NLO30 fit	experiment
γ	2.36	2.37	2.36(4)
R_c	0.656	0.660	0.664(11)
R_n	0.207	0.191	0.189(15)
$\Delta E_N(1s)$ [eV]	307	310	283(42)
$\Gamma(1s)$ [eV]	590	607	541(111)
z_1 [MeV]	(1353,-43)	(1355,-86)	$\Lambda_1(1405)$
z_2 [MeV]	(1429,-24)	(1418,-44)	$\Lambda_2(1405)$
z_3 [MeV]	(1677,-14)	(1774,-35)	$\Lambda(1670)$

We conclude the presentation of our new $\bar{K}N$ model by demonstrating the energy dependence of the K^-p elastic amplitude. This is done in Fig. 2 where our results are shown in comparison with those generated by the NLO30 model and the Kyoto-Munich model [14]. Interestingly, our current model provides the K^-p energy dependence very similar to the one obtained by the latter approach. Considering the fact that the higher energy cross sections were not included in the analysis performed in [14] and there are more instances where the two models differ (e.g. by a use of separable

potentials in our approach) the agreement of the two models seems to be rather coincidental.

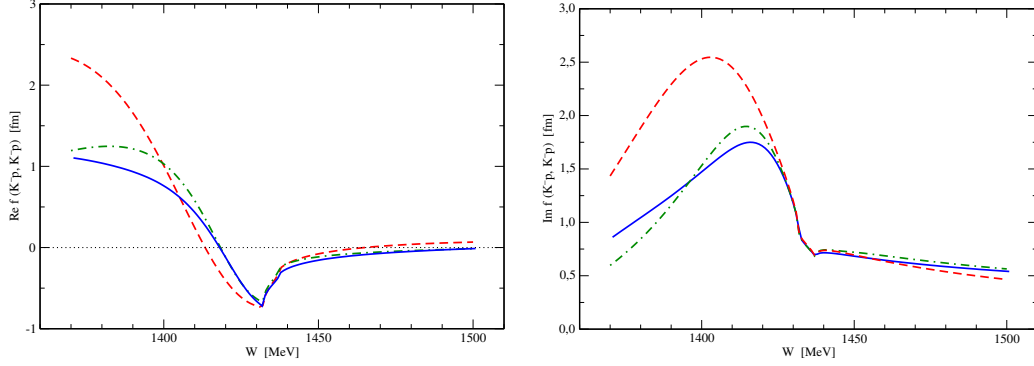


Figure 2: Energy dependence of the K^-p amplitude. The real and imaginary parts of the amplitude are shown in the left and right panels, respectively. Continuous blue lines represent our current model predictions, the dashed red lines the predictions of the NLO30 Prague model, and the dot-dashed green lines the predictions of the Kyoto-Munich model.

3. SU(3) flavor symmetry in coupled-channel models

In what follows we consider only the fully flavor-symmetric case of s -wave $S = -1$ MB scattering, where the meson and the baryon are members of the respective ground-state octets. From the tensor product decomposition of multiplets, $\mathbf{8} \otimes \mathbf{8} = \mathbf{1} \oplus \mathbf{8} \oplus \mathbf{8} \oplus \mathbf{10} \oplus \overline{\mathbf{10}} \oplus \mathbf{27}$, one expects s -channel exchanges of singlet, octet, decuplet and 27-plet resonances in such a process. As there are no decuplet states with charge $Q = 0$, $S = -1$, $I = L = 0$, we can disregard them for our purposes. The relevant MB states for our study are (see Appendix B of [20] for our phase conventions)

$$\begin{aligned}
 |\pi\Sigma\rangle_{I=0} &= -\frac{1}{\sqrt{3}} (|\pi^0\Sigma^0\rangle + |\pi^-\Sigma^+\rangle + |\pi^+\Sigma^-\rangle) , \\
 |\bar{K}N\rangle_{I=0} &= -\frac{1}{\sqrt{2}} (|\bar{K}^0n\rangle + |K^-p\rangle) , \quad |\eta\Lambda\rangle_{I=0} = |\eta\Lambda\rangle , \\
 |K\Xi\rangle_{I=0} &= \frac{1}{\sqrt{2}} (|K^0\Xi^0\rangle + |K^+\Xi^-\rangle) .
 \end{aligned} \tag{6}$$

From these one can construct the following set of MB flavor eigenstates:

$$\begin{aligned}
|(\mathbf{1})\rangle_{I=0} &= \frac{1}{\sqrt{8}} \left(|\eta\Lambda\rangle_{I=0} - \sqrt{2}|\bar{K}N\rangle_{I=0} + \sqrt{2}|K\Xi\rangle_{I=0} - \sqrt{3}|\pi\Sigma\rangle_{I=0} \right), \\
|(\mathbf{8})\rangle_{I=0} &= \frac{1}{\sqrt{10}} \left(\sqrt{2}|\eta\Lambda\rangle_{I=0} - |\bar{K}N\rangle_{I=0} + |K\Xi\rangle_{I=0} + \sqrt{6}|\pi\Sigma\rangle_{I=0} \right), \quad (7) \\
|(\mathbf{8}')\rangle_{I=0} &= \frac{1}{\sqrt{2}} (|\bar{K}N\rangle_{I=0} + |K\Xi\rangle_{I=0}), \quad (8) \\
|(\mathbf{27})\rangle_{I=0} &= \frac{1}{\sqrt{40}} \left(3\sqrt{3}|\eta\Lambda\rangle_{I=0} + \sqrt{6}|\bar{K}N\rangle_{I=0} - \sqrt{6}|K\Xi\rangle_{I=0} - |\pi\Sigma\rangle_{I=0} \right).
\end{aligned}$$

A quick and straightforward way to obtain symmetry constraints for the couplings of possible Λ^* resonances to the above states is given by writing down effective chiral Lagrangians containing *explicit* fields pertaining to the Λ^* states. For a singlet and an octet Λ^* , respectively, one can adopt

$$\mathcal{L}_Y^{(\mathbf{1})} = \frac{D_S}{2} \langle \bar{B} \gamma^\mu u_\mu \rangle \Lambda^* + h.c., \quad (9)$$

$$\mathcal{L}_Y^{(\mathbf{8})} = \frac{D_Y}{2} \langle \bar{B} \gamma^\mu \{u_\mu, Y\} \rangle + \frac{F_Y}{2} \langle \bar{B} \gamma^\mu [u_\mu, Y] \rangle + h.c., \quad (10)$$

where $Y = \frac{1}{\sqrt{6}} \text{diag}(1, 1, -2) \Lambda^* + (\text{other fields})$, u^μ and B contain the meson and baryon octet fields in the usual fashion (compare e.g. Appendix A of [20] for our notation), and D_S, D_Y, F_Y are coupling constants. We shall not encounter a 27-plet resonance, so we omit a corresponding effective Lagrangian here (see, however, Eq. (4.24) in [40]). For a later reference, we also provide an example of an application of the above Lagrangians: From $\mathcal{L}_Y^{(\mathbf{1})}$, one derives the tree-level contribution to the $I = 0$ s-wave amplitude for $\pi\Sigma$ scattering due to an s -channel exchange of a singlet Λ^* hyperon as

$$f_{0+, I=0}^{(\text{tree})}(\pi\Sigma \rightarrow \pi\Sigma) = -\frac{3D_S^2 (E_\Sigma + m_\Sigma) (\sqrt{s} - m_\Sigma)^2}{2F_\pi^2 8\pi\sqrt{s} \sqrt{s} - m_{\Lambda^*}}. \quad (11)$$

We do not incorporate such graphs with explicit resonances in our model, but only use them to illustrate some general features of the resonance-pole terms from a different viewpoint. Specifically, we focus on ratios of moduli of couplings β that determine how strongly the MB channels couple to a specific Λ^* state, see Eq. (16) below as well. We anticipate that in these ratios the conventional prefactors and phases drop out. With the help of the

above formalism, for the singlet case one deduces

$$\begin{aligned} r_{12} &:= \left| \frac{\beta(\Lambda^* \rightarrow \pi\Sigma)}{\beta(\Lambda^* \rightarrow \bar{K}N)} \right| = \sqrt{\frac{3}{2}}, & r_{13} &:= \left| \frac{\beta(\Lambda^* \rightarrow \pi\Sigma)}{\beta(\Lambda^* \rightarrow \eta\Lambda)} \right| = \sqrt{3}, \\ r_{24} &:= \left| \frac{\beta(\Lambda^* \rightarrow \bar{K}N)}{\beta(\Lambda^* \rightarrow K\Xi)} \right| = 1, \end{aligned} \quad (12)$$

while for an octet Λ^* , the corresponding ratios are of the form

$$r_{12} = \left| \frac{D_Y}{D_Y + 3F_Y} \right|, \quad r_{13} = \sqrt{3}, \quad r_{24} = \left| \frac{D_Y + 3F_Y}{D_Y - 3F_Y} \right|, \quad (13)$$

and finally for a 27-plet member,

$$r_{12} = \frac{1}{\sqrt{6}}, \quad r_{13} = \frac{1}{3\sqrt{3}}, \quad r_{24} = 1. \quad (14)$$

Relations like this are, of course, well-known - we compile them here just for an easy comparison with our results presented in the next section. In Appendix A, we collect the formulae used to map out the trajectory from the *real world* setting to a conveniently chosen symmetric one. Before we go on to apply the above analysis to our coupled-channel formalism, we have to make a remark on the octet states. In general, a Λ^* octet state will couple to a mixture of the two octet states introduced in Eqs. (7-8), parameterized by an angle θ . Taking this into account, we expect one of

$$\begin{aligned} |(1)\rangle &\equiv |(1)\rangle_{I=0}, & |(27)\rangle &\equiv |(27)\rangle_{I=0}, \\ |(\mathbf{8a})\rangle &= \cos\theta |(\mathbf{8})\rangle_{I=0} - \sin\theta |(\mathbf{8}')\rangle_{I=0}, \\ |(\mathbf{8b})\rangle &= \sin\theta |(\mathbf{8})\rangle_{I=0} + \cos\theta |(\mathbf{8}')\rangle_{I=0}, \end{aligned}$$

to be the MB state coupled to an s -channel resonance generated in our framework. More generally, in case of exact flavor symmetry the 4×4 coupled channel matrix v containing our interaction kernel must be diagonalized by an orthogonal matrix of the form

$$\mathcal{S} = \left(\begin{array}{c|c|c|c} -\sqrt{\frac{3}{8}} & \sqrt{\frac{6}{10}} \cos\theta & \sqrt{\frac{6}{10}} \sin\theta & -\frac{1}{\sqrt{40}} \\ -\sqrt{\frac{2}{8}} & -\frac{\cos\theta}{\sqrt{10}} - \frac{\sin\theta}{\sqrt{2}} & -\frac{\sin\theta}{\sqrt{10}} + \frac{\cos\theta}{\sqrt{2}} & \sqrt{\frac{6}{40}} \\ \frac{1}{\sqrt{8}} & \sqrt{\frac{2}{10}} \cos\theta & \sqrt{\frac{2}{10}} \sin\theta & 3\sqrt{\frac{3}{40}} \\ \sqrt{\frac{2}{8}} & \frac{\cos\theta}{\sqrt{10}} - \frac{\sin\theta}{\sqrt{2}} & \frac{\sin\theta}{\sqrt{10}} + \frac{\cos\theta}{\sqrt{2}} & -\sqrt{\frac{6}{40}} \end{array} \right), \quad (15)$$

i.e. $v = \mathcal{S}v_{\text{diag}}\mathcal{S}^\top$, where $v_{\text{diag}} = \text{diag}(v_{(1)}, v_{(\mathbf{8a})}, v_{(\mathbf{8b})}, v_{(\mathbf{27})})$. In the generic case, when $v_{(\mathbf{8a})} \neq v_{(\mathbf{8b})}$, it should be possible to determine the angle θ (at a given energy) from this requirement. However, for $v_{(\mathbf{8a})} = v_{(\mathbf{8b})}$, e.g. for a pure WT kernel, this is not possible. In this particular case the degeneracy appears due to an *accidental symmetry* of the WT kernel. Since our full scattering amplitude is given in a form of a geometric series, $t = v + vGv + vGvGv + \dots$, composed from the interaction kernel v and the diagonal matrix G containing only one universal loop function for all four channels in the SU(3)-symmetric case ($G \sim \mathbf{1}_{4 \times 4}$), it is clear that $t = \mathcal{S}(\text{diag}(t_{(1)}, t_{(\mathbf{8a})}, t_{(\mathbf{8b})}, t_{(\mathbf{27})}))\mathcal{S}^\top$ too. Thus, we can extract the coupling ratios for a given resonance (or a bound state) from the pertinent pole residues of the t -matrix, and classify the resonances uniquely according to their flavor content.

In the real world, the flavor symmetry is broken and, unfortunately, things are not so simple. Even if the flavor-breaking effects in the interaction kernel are small, the loop functions will be different in each channel, and we have to deal with 2^n Riemann sheets (RSs) of the complex energy surface (for n channels), where the G entries can be different depending on their threshold energies. This will introduce a *kinematical flavor breaking* for resonances located on a sheet with mixed signature, i.e. with different signs of the imaginary parts of the various loop functions. Thus, the symmetry constraints discussed above will not apply to a pole located on a RS with a mixed signature, even in the limit of zero flavor breaking. However, as the interval on the physical real axis connecting the *mixed* sheet and the physical sheet shrinks to a point when this limit is approached, the resonance also becomes *unphysical* (i.e. unobservable). In this way, an apparent contradiction between measurable resonance properties and exact flavor symmetry is avoided. We shall see examples of such behavior in the next section. In addition, even if a resonance pole ends up on the physical RS (as a bound state), or the unphysical RS connected to it in the symmetry limit, it can switch over from one sheet to another for a certain value of the flavor breaking, in which case the coupling ratios can vary quite dramatically. While it is hard to judge how *realistic* such scenarios are, these observations point to the fact that a smooth dependence on the flavor breaking, and a simple connection to the fully SU(3)-symmetric scenario, is not guaranteed for all resonances generated in a multi-channel system.

4. Results and discussion

In this section we discuss how the broken SU(3) flavor symmetry affects the properties of dynamically generated resonances that are observed in the isoscalar $S = -1$ sector. The chirally motivated coupled channel model introduced in Sec. 2 generates two resonant states assigned to $\Lambda(1405)$ and another one to the $\Lambda(1670)$ resonance, see Table 2 for the positions of the pertinent poles at complex energies $z = \sqrt{s}$. These poles are located at RSs that would be called *the second RS* if only two channels were considered, e.g. on the RS that is connected with the physical region at the real axis around the given pole energy $\text{Re } z$. In our notation, they are the $[-, +, +, +]$ and $[-, -, -, +]$ RS for the $\Lambda(1405)$ and the $\Lambda(1670)$ poles, respectively. We remark that the appearance of the resonances on the RSs that are not completely symmetric with respect to all coupled channels is a consequence of the broken SU(3) flavor symmetry in the physical limit. As we will see one can gradually restore the SU(3) symmetry and track the movement of the poles. However, as we already indicated at the end of the previous section, it is not guaranteed that the pole will reside on a channel symmetric RS (either all channel momenta physical or all of them unphysical) when one reaches the SU(3) flavor limit this way.

The movement of the poles from (or to) the SU(3) flavor limit was already explored in [11]. In the present work we follow a similar procedure by introducing a scaling parameter x but opt for a slightly different approach to the variations of the hadron masses and other model parameters (decay constants F_j and inverse ranges α_{jb}) when defining the trajectory from the limit of restored SU(3) flavor symmetry (at $x = 0$) to the physical limit (at $x = 1$), see Appendix A for details. When going from the physical limit by restoring gradually the SU(3) flavor symmetry we follow the movement of the poles as well as the ratios of the channel couplings r_{ij} introduced in Eqs. (12-14) in the previous section. The couplings β_{jb} that are required for the ratios can be calculated as residua of the scattering amplitude,

$$\text{Res}_{z=z_R} f_{ia,jb}(z) = \beta_{ia} \beta_{jb} . \quad (16)$$

Referring back to the example given in Eq. (11), we do not expect any phase-space factors $\sim q(s)$ contained in the couplings β . The coupling factors are also related to the *compositeness* \mathcal{C} of the dynamically generated state

assigned to the pertinent pole [41, 42, 43, 44] via

$$\mathcal{C}_{jb}(z_R) = \beta_{jb}^2 \frac{dG_{jb}}{dz}(z_R), \quad (17)$$

where the loop function $G(z)$ is the one introduced in Eq. (4).

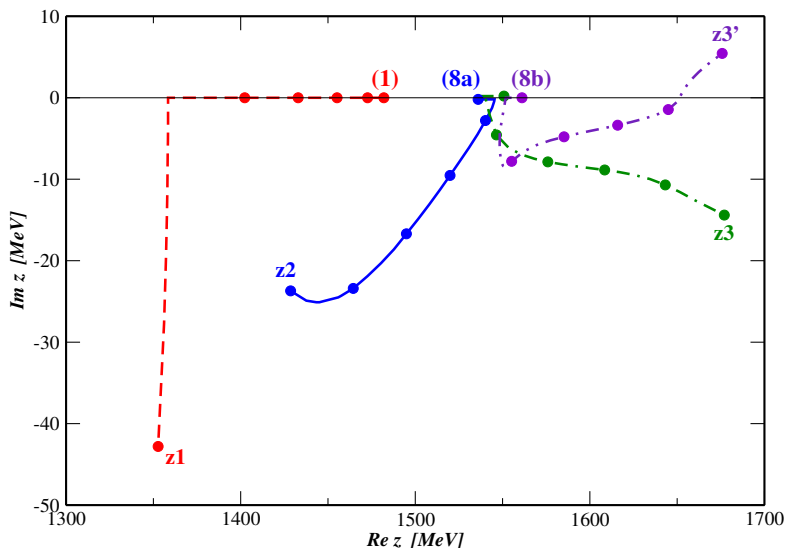


Figure 3: Movements of the poles upon varying the x parameter that scales the breaking of the SU(3) flavor symmetry. The pole positions in the physical limit ($x = 1$) are marked as z_1 , z_2 and z_3 , the circles on the pole trajectories indicate the positions of the poles for x values modified in steps of 0.2. See text for explanation on the shadow z_3' pole and more details.

At first, let us have a look at the movement of the poles as one goes from the physical limit to the point of the restored SU(3) flavor symmetry. The pole trajectories are shown in Fig. 3 and the starting positions (for $x = 1$) of the z_1 , z_2 and z_3 poles are exactly those given in Table 2. As we gradually decrease the scaling parameter x from 1 to 0 the poles move along their respective paths reaching (for $x = 0$) the end points located at the real axis. We also mark by full circles the pole positions at x values that are multiples of 0.2, so one can judge how fast the poles move. The trajectory of the z_1 pole (the *lower mass* $\Lambda_1(1405)$ pole) is visualized by the red dashed line in the figure. As the x value is reduced the pole moves very fast to reach the real axis for $x = 0.9$, then continues to move along it to reach its final position at the energy $z_{(1)} = 1482$ MeV, a point we identify as a SU(3) flavor

singlet. As the z_1 pole moves along the real axis it also switches from the $[-, +, +, +]$ RS to the $[+, +, +, +]$ RS which happens for $x = 0.85$ when the pole catches on the lowest $\pi\Sigma$ threshold (that also keeps moving when we vary x). The movement of the z_2 pole (the *higher mass* $\Lambda_2(1405)$ one) is visualized by the continuous blue line and we find it more fluid with a major part of its trajectory on the $[-, +, +, +]$ RS. The pole reaches the real axis for $x = 0.11$, immediately hits the lowest threshold and switches to the physical $[+, +, +, +]$ RS ending its movement (for $x = 0$) at the energy $z_{(\mathbf{8a})} = 1536$ MeV, a point we associate with one of the SU(3) octets. Thus, each of the two $\Lambda(1405)$ poles goes to a different state in the SU(3) flavor limit, both states located on the physical RS (in all channels).

Although the $\Lambda(1670)$ related z_3 pole trajectory in Fig. 3, (see the green dot-dashed line there) is quite similar to the z_2 pole movement the situation is more complicated in this case. The pole spends most of its movement on the $[-, -, -, +]$ RS, reaches the real axis at $x = 0.15$, slightly below the lowest $\pi\Sigma$ threshold but when it hits this threshold it ends up on the $[+, -, -, +]$ RS. Although the pole movement ends on the real axis, the RS is not channel symmetric, so the final point of the z_3 pole trajectory cannot be identified with any SU(3) flavor symmetric state. In fact, we were able to locate the second SU(3) octet pole at the (all channels physical) $[+, +, +, +]$ RS at the energy $z_{(\mathbf{8b})} = 1561$ MeV. Thus, the z_3 pole movement apparently aims at this **(8b)** state, but ends at the energy $z_3(x = 0) = 1551$ MeV, 10 MeV below the **(8b)** state and on a different RS.

Of course, the pole movement can also be followed in the opposite way, starting from the pole position found for $x = 0$ and increasing gradually the x value. When one does so for the **(8b)** octet state we get the pole trajectory shown by the magenta dot-dot-dashed line in Fig. 3. The pole movement starts on the physical $[+, +, +, +]$ RS, then switches to the $[-, +, +, +]$ RS, leaves the real axis, and finally crosses the real axis in between the (moving) $\eta\Lambda$ and $K\Xi$ thresholds switching to the $[+, -, -, +]$ RS, where it ends its movement at the complex energy $z'_3 = (1676, 5.4)$ MeV. We have checked the origin of this pole by looking at its movement to the zero coupling limit (ZCL) in which the inter-channel couplings are switched off. In this limit, both the z_3 and z'_3 poles coalesce and are represented by the same $K\Xi$ bound state, thus the two poles originate from the same ZCL state and represent shadow poles to each other in the physical limit, see Refs. [45], [46] and [47] for more details on the the ZCL and the concept of shadow poles. In the physical limit, the z_3 and z'_3 poles are both located at very similar energies

(do note they both have partners at complex conjugated energies) but since the z'_3 pole resides on a more distant RS, it is the z_3 pole that appears relevant for any physical observables and can be assigned to the $\Lambda(1670)$ resonance. Nevertheless, both these poles have the same origin in the ZCL and both of them go to the **(8b)** octet state when $x \rightarrow 0$, the z'_3 pole manages to get exactly there while the track of the z_3 pole gets only close to the **(8b)** pole position due to ending up on a different (not fully symmetric) RS.

Let us continue with discussing the ratios of the channel couplings introduced in Eqs. (12-14). Table 3 provides the ratios for all four discussed poles and three SU(3) scaling parameter values, $x = 0, 0.5$ and 1. When one checks the rates for $x = 0$ and compares them with the predictions made in the previous section we confirm our preliminary assignment of the SU(3) flavor singlet and octet states to the pole positions in this limit. In particular, it is the z'_3 pole trajectory that clearly goes to the SU(3) octet state while the $z_3(x = 0)$ rates do not comply with any of the predictions given in Eqs. (12-14). Referring to the parameters entering Eq. (13), we find from the ratios r_{12}, r_{24} at $x = 0$ that $F_Y(z_2)/D_Y(z_2) \approx -1.439$ and $F_Y(z'_3)/D_Y(z'_3) \approx 0.357$, the product of the latter two ratios being ≈ -0.514 (for which one would expect $-5/9$ from the decomposition of the two orthogonal octet states, if the two states were exactly mass-degenerate).

Table 3: The couplings ratios r_{ij} for $x = 0, 0.5$ and 1.

pole	x	r_{12}	r_{13}	r_{24}	pole	x	r_{12}	r_{13}	r_{24}
z_1	0.0	1.225	1.732	1.000	z_2	0.0	0.739	1.732	0.624
	0.5	0.985	2.768	6.861		0.5	0.826	1.559	3.805
	1.0	1.380	5.542	19.04		1.0	0.659	1.635	17.53
z_3	0.0	3.417	3.120	4.154	z'_3	0.0	1.182	1.732	28.63
	0.5	0.730	0.507	0.202		0.5	1.538	0.576	0.175
	1.0	0.974	0.393	0.156		1.0	1.208	0.440	0.152

In the physical limit ($x = 1$) our results are in agreement with observations made in many previous papers, see e.g. [17, 18, 47, 48]. The z_1 pole couples most strongly to the $\pi\Sigma$ channel, though its coupling to the $\bar{K}N$ channel is also large. The couplings to the z_2 pole are dominated by the

$\bar{K}N$ channel and the couplings to the z_3 (as well as the z'_3) pole by the $K\Xi$ channel. Obviously, for all three poles the largest (and most significant) is the coupling to the channel from which the pole originates in the ZCL [47]. However, as the latter statement is true in the physical limit the same cannot be said in the SU(3) flavor limit. There, all four $I = 0$ channels couple strongly to the z_1 and z_2 poles that turn into the SU(3) singlet and octet states for $x \rightarrow 0$, respectively. On the other hand, the z_3 pole is dominated by couplings to the $\pi\Sigma$ channel, and the $K\Xi$ coupling is marginalized for small x values. For both the z_3 and z'_3 poles, it is remarkable how the coupling of the $K\Xi$ channel changes from a dominant one in the physical limit to a marginalized one in the limit of restored SU(3) flavor symmetry. In quite an opposite manner, the couplings of the same $K\Xi$ channel to the z_1 and z_2 poles change dramatically from negligible ones to being comparable with those of other channels when one goes from the physical to the SU(3) symmetric limit. For these two $\Lambda(1405)$ poles, in Fig. 4 we demonstrate the whole dependence of the r_{ij} ratios on the scaling parameter x . There, it can be seen that while the r_{12} value (equal to the ratio of $\pi\Sigma$ and $\bar{K}N$ couplings) remains reasonably stable, the r_{24} value (ratio of $K\Xi$ and $\bar{K}N$ couplings) changes dramatically. We point out that such behavior cannot be explained by considering any associated phase-space factors that might impact on the r_{ij} ratios.

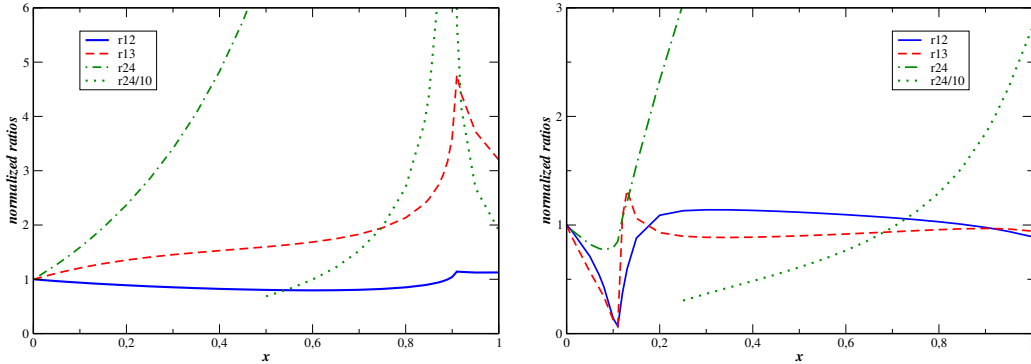


Figure 4: Dependence of the ratios r_{12} , r_{13} and r_{24} on the x factor used to scale the breaking of the SU(3) flavor symmetry. The ratios are normalized to their values at $x = 0$. Left panel - the z_1 pole, right panel - z_2 pole.

To complement our analysis of the poles and the channel couplings we present our predictions for the compositeness of the dynamically generated

states, see Eq. (17), for both the $x = 0$ and $x = 1$ limits. Our results are shown in Tables 4 and 5. For the $x = 0$ case, the reader can easily check that the simple rules $|\mathcal{C}_{\pi\Sigma}/\mathcal{C}_{\bar{K}N}| = 3/2$ and $|\mathcal{C}_{K\Xi}/\mathcal{C}_{\bar{K}N}| = 1$ apply for the singlet state, and $|\mathcal{C}_{\pi\Sigma}/\mathcal{C}_{\eta\Lambda}| = 3$ for both singlet and octet states, compare Eqs. (12), (13) and (17). Turning to the $x = 1$ case, it is seen that the aforementioned ratios deviate strongly from these SU(3) predictions. While we refrain here from joining the debate on the (probabilistic) interpretation of the \mathcal{C}_{jb} values (see e.g. [44, 49, 50, 51]), we just point out that the state related to the $\Lambda_2(1405)$ pole z_2 is apparently dominated by a $\bar{K}N$ molecular component ($|\mathcal{C}_{\bar{K}N}(z_2)| \approx 0.97$), whereas the state related to z_1 is dominated by a $\pi\Sigma$ component ($|\mathcal{C}_{\pi\Sigma}(z_1)| \approx 0.65$). The higher-lying channels seem to play only a minor role in the composition of these states, but take a somewhat bigger part in the formation of the states related to z_3 and z'_3 . These findings are in good qualitative agreement with earlier studies, compare e.g. Table 1 in [44], Table 1 in [52] and Table 4 in [53].

Table 4: Pole couplings and compositeness in the SU(3) flavor limit, for $x = 0$.

pole		z_1	z_2	z_3	z'_3
\sqrt{s} [MeV]		(1482, 0)	(1536, 0)	(1551, 0)	(1561, 0)
RS		[+, +, +, +]	[+, +, +, +]	[+, -, -, +]	[+, +, +, +]
$\pi\Sigma$	$ \beta_{jb} $	0.479	0.226	0.629	0.222
	\mathcal{C}_{jb}	(0.205, 0.000)	(0.099, 0.)	(1.244,-0.000)	(0.484,-0.000)
	$ \mathcal{C}_{jb} $	0.205	0.099	1.244	0.484
$\bar{K}N$	$ \beta_{jb} $	0.391	0.306	0.184	0.188
	\mathcal{C}_{jb}	(0.136, 0.000)	(0.181, 0.000)	(-0.134, 0.)	(0.347, 0.000)
	$ \mathcal{C}_{jb} $	0.136	0.181	0.134	0.347
$\eta\Lambda$	$ \beta_{jb} $	0.277	0.130	0.202	0.128
	\mathcal{C}_{jb}	(0.068, 0.000)	(0.033, 0.000)	(-0.160, 0.000)	(0.161, 0.000)
	$ \mathcal{C}_{jb} $	0.068	0.033	0.160	0.161
$K\Xi$	$ \beta_{jb} $	0.391	0.490	0.044	0.007
	\mathcal{C}_{jb}	(0.136, 0.000)	(0.464, 0.000)	(0.006, 0.000)	(0.000, 0.000)
	$ \mathcal{C}_{jb} $	0.136	0.464	0.006	0.000

Table 5: Pole couplings and compositeness in the physical limit, for $x = 1$.

pole		z_1	z_2	z_3	z'_3
\sqrt{s} [MeV]		(1353, -43)	(1429, -24)	(1677, -14)	(1676, 5)
RS		[-, +, +, +]	[-, +, +, +]	[-, -, -, +]	[+, -, -, +]
$\pi\Sigma$	$ \beta_{jb} $	0.670	0.433	0.096	0.118
	\mathcal{C}_{jb}	(0.323, 0.565)	(0.072, -0.208)	(-0.003, -0.009)	(-0.007, -0.012)
	$ \mathcal{C}_{jb} $	0.651	0.220	0.009	0.014
$\bar{K}N$	$ \beta_{jb} $	0.486	0.656	0.099	0.097
	\mathcal{C}_{jb}	(-0.101, -0.176)	(0.957, 0.132)	(0.010, -0.004)	(0.000, 0.010)
	$ \mathcal{C}_{jb} $	0.203	0.966	0.011	0.010
$\eta\Lambda$	$ \beta_{jb} $	0.121	0.265	0.245	0.267
	\mathcal{C}_{jb}	(-0.005, -0.001)	(0.028, 0.012)	(-0.024, 0.192)	(-0.019, -0.268)
	$ \mathcal{C}_{jb} $	0.005	0.030	0.194	0.269
$K\Xi$	$ \beta_{jb} $	0.026	0.037	0.633	0.640
	\mathcal{C}_{jb}	(0.000, 0.000)	(0.000, 0.000)	(0.276, -0.083)	(0.276, 0.097)
	$ \mathcal{C}_{jb} $	0.000	0.000	0.288	0.293

Let us compare our findings with an earlier analysis by D. Jido et. al. [11] and discuss a possible model dependence of our results. First of all, it should be noted that in Ref. [11] only the WT term was considered when constructing the effective coupled-channel interaction potentials. In this setting the two SU(3) octet states merge into one and both, the z_2 and z_3 poles head to the same state when the SU(3) flavor symmetry is gradually restored. Our results for the Λ^* related poles confirm the observations made in [11], the $\pi\Sigma$ related (in terms of its origin in ZCL) $\Lambda_1(1405)$ pole goes to the SU(3) singlet state, while the $\bar{K}N$ related $\Lambda_2(1405)$ pole and the ($K\Xi$ related) $\Lambda(1670)$ pole go to the octet state. However, as our MB interaction is not restricted to the WT term, we were able to demonstrate that the two latter poles go to the **(8a)** and **(8b)** octets, respectively. Thus, each of the three Λ^* states goes to a different SU(3) flavor symmetric state. The exact positions of the **(8a)** and **(8b)** octet states depend on the diagonalized effective potentials $v_{(8a)}$ and $v_{(8b)}$, and on the inverse range $\alpha_0 = \alpha_{jb}(x = 0)$. In fact, for the

Prague NLO30 [16] and the current model the positions of the poles $z_{(\mu)}$, where (μ) stands for the singlet **(1)** or for the octets **(8a)** and **(8b)**, can be found as a solution of Eq. (17) in [47] in which the common inverse range α_0 and pertinent SU(3) symmetric μ -state quantities are to be used instead of the n -th channel ones. We have checked that the two octet poles **(8a)** and **(8b)** indeed merge if we gradually switch off the Born and NLO terms contributing to the potentials $v_{(\mathbf{8a})}$ and $v_{(\mathbf{8b})}$. For the parameter setting of our current model the adopted value $\alpha_0 = 750$ MeV is also sufficiently large to generate both **(8a)** and **(8b)** poles on the physical $[+, +, +, +]$ RS, with the **(8b)** pole energy $z_{(\mathbf{8b})} = 1561.1$ MeV just below the common MB threshold $\sqrt{s_{thr}} = m_N(x=0) + M_K(x=0) = 1562.6$ MeV. If the α_0 value was larger, all SU(3) symmetric μ -states would be more bound and the pertinent poles would be located at smaller energies. On the other hand, smaller values of α_0 lead to weaker binding and for $\alpha_0 = 700$ MeV the **(8b)** pole effectively reaches the threshold, being located marginally (by 0.03 MeV) below it. For even smaller values of α_0 the **(8b)** pole moves to the unphysical $[-, -, -, -]$ RS and becomes a virtual SU(3) symmetric octet state.

The sensitivity of the SU(3) multiplets pole positions to the chosen α_0 value may raise some concerns. The same can be said about the *natural value* $a_0 \approx -2$ adopted in [11] for a subtraction constant used in 3d regularization of the MB loop integrals in the flavor symmetric limit. In Table 6 we show the SU(3) flavor symmetric scattering lengths a_μ at the common MB threshold $\sqrt{s_{thr}}$. The presented values were obtained by transforming the scattering length matrix $a_{ia,jb} = f_{ia,jb}(\sqrt{s_{thr}})$ into a diagonal form with the help of Eq. (15). There is a notable sensitivity of the value of a_μ to α_0 , especially for the octet components. In particular, we note that the extremely large value of $a_{(\mathbf{8b})}$ for $\alpha_0 = 700$ MeV is due the **(8b)** pole position being practically at the threshold. Naturally, all the scattering lengths get smaller as the pole positions move down (to lower energies), away from the threshold, when α_0 increases. In principle, it should be possible to calculate the MB scattering lengths at a flavor-symmetric point within Lattice QCD [54, 55, 56, 57, 58]. Such data would certainly be helpful to fix the parameter α_0 in our model. Presently, however, we can only offer an estimated range for our predictions, as given in Table 6.

We have also tested the model dependence by performing the same analysis with the Prague NLO30 model [16]. As the model setting (chiral Lagrangian treatment, NLO couplings) is different, so are the pole positions in both, the physical as well as in the SU(3) flavor symmetric limit. In par-

Table 6: The SU(3) flavor symmetric scattering lengths $a_{(\mu)}$, calculated for $x = 0$ at the common meson-baryon threshold energy $\sqrt{s_{thr}} = 1562.6$ MeV. The results are presented for three choices of the common regularization scale, the inverse range parameter α_0 .

α_0 [MeV]	$a_{(\mathbf{1})}$ [fm]	$a_{(\mathbf{8a})}$ [fm]	$a_{(\mathbf{8b})}$ [fm]	$a_{(\mathbf{27})}$ [fm]
700	-1.007	-1.912	-46.861	-0.248
750	-0.893	-1.539	-6.755	-0.240
800	-0.802	-1.288	-3.640	-0.233

ticular, the **(8b)** octet pole is located on the $[-, -, -, -]$ RS as a virtual state just below the MB threshold $\sqrt{s_{thr}}$ when we use the $\alpha_0 = 750$ MeV value. Otherwise, the NLO30 model is in a nice qualitative agreement with the current model: the $\pi\Sigma$ and $\bar{K}N$ related $\Lambda(1405)$ poles go to the SU(3) singlet and **(8a)** octet states, respectively, and the $K\Xi$ related $\Lambda(1670)$ pole goes to the **(8b)** octet state but ends up (for $x = 0$) on a RS that is not completely channel symmetric. Exactly as in our current model, it is a shadow $K\Xi$ related pole that originates from the **(8b)** octet state.

Finally, we mention that both our current and the NLO30 Prague model generate dynamically three poles in the isovector sector. The existence of such poles in the physical limit was discussed in [47] and we checked that upon restoring the SU(3) flavor symmetry these poles go to the same SU(3) singlet and octet states as do the Λ^* poles found in the isoscalar sector. A similar observation was made in [11], though the trajectories of only two isovector poles were followed there. Unfortunately, the isovector sector is not restricted much by the current experimental data on $\bar{K}N$ interactions, so any predictions made for it are strongly model dependent and not very reliable. For this reason, we refrain from discussing any dynamically generated Σ^* states within the SU(3) flavor symmetry context, at least for the time being. The situation may change with appearance of new experimental data in the near future, e.g. those from measurements of kaonic deuterium data [59] or on the K_L^0 reactions [60].

5. Summary and conclusions

In this contribution, we have presented an updated version of the model detailed in [16] and [61], modified in the spirit of our recent work on ηN and $\eta' N$ interactions [20]. As we have demonstrated, we arrived at a satisfying description of the $I = 0$, $S = -1$ MB s-wave scattering processes in the $\Lambda(1405)$ as well as in the $\Lambda(1670)$ resonance regions. This achievement enabled us to analyze the variations of the pole positions and couplings to the Λ^* states when the flavor-symmetry breaking terms in our model are continuously switched off. It is worth pointing out that we necessarily need a good control over the amplitude in the $\Lambda(1670)$ region to study this variation with some confidence, because the aforementioned resonances move close together when approaching the flavor-symmetry limit (see our Fig. 3 and compare also Fig. 1 in [11]), forming one dense cluster of near-threshold resonances that is disentangled only by turning on the symmetry breaking. It is reassuring to see that the flavor classification of the resonances agrees with the earlier analysis performed in [11] employing only the WT interaction kernel and a somewhat different construction of the coupled-channel amplitude. Our use of a higher-order kernel allows us not only to confirm these findings, but also facilitates a more detailed resolution of the pole structure of the amplitude, applicable to a wider energy range.

Our observations, described in the previous section, also warn us of an imprudent application of SU(3)-based estimates to resonances in a multi-channel scattering problem: As the couplings of the channels (and their ratios) to the dynamically generated resonances can vary quite dramatically when going from the physical situation to the limit of restored SU(3) flavor symmetry, the couplings determined from physical observables cannot be used immediately to reliably identify the flavor multiplet to which the resonance in question is (predominantly) associated. At least in some complicated cases, it seems necessary to follow the whole path of the pertinent pole upon gradually restoring the flavor symmetry to establish the pole origin in a proper way. In this respect, our findings put under question any such assignments made purely on the basis of partial wave analyses of the experimental data, e.g. in the one performed recently in [62]. In particular, we have demonstrated the possibility that the trajectory of some resonance pole ends up (for $x = 0$) on a sheet labeled with a mixed signature, to which the usual SU(3) estimates do not even apply in the fully symmetric situation. Though, one could probably develop generalized symmetry relations

for such cases. To our knowledge, such a possibility is not widely discussed in the literature on applications of SU(3) symmetry to hadron physics. Of course, we must mention here that, while we have obtained a good description of the scattering data, our amplitude is not well constrained near the unphysical point $x = 0$. There, our results should be seen as a tentative prediction. In principle, this situation could be improved by an evaluation of the $S = -1$ baryon spectrum around a flavor-symmetric point within Lattice QCD, following e.g. the strategy presented in [57, 58]. Up to now, however, we have to rely on the emergence of a consistent picture from comparisons with alternative models for $\bar{K}N$ scattering. Further comparative studies in this direction are left for future publications.

Acknowledgement

This work was supported by the Czech Science Foundation GACR grant 19-19640S.

Appendix A. Trajectory from the symmetric limit to the physical point

The flavor-symmetric limit we consider in this work is specified by the formulae below. The trajectory to the physical point is defined by varying the parameter $x = 0 \dots 1$ in a way that the average quark mass $\frac{1}{3}(m_u + m_d + m_s)$ stays (approximately) constant. We can achieve this by using the following prescriptions:

$$\begin{aligned}
M_\pi^2(x) &= \frac{1}{3}(2M_K^2 + M_\pi^2) - \frac{2x}{3}(M_K^2 - M_\pi^2) , \\
M_K^2(x) &= \frac{1}{3}(2M_K^2 + M_\pi^2) + \frac{x}{3}(M_K^2 - M_\pi^2) , \\
M_\eta^2(x) &= \frac{1}{3}(2M_K^2 + M_\pi^2) + \frac{x}{3}(3M_\eta^2 - (2M_K^2 + M_\pi^2)) , \\
m_N(x) &= \frac{1}{3}(m_N + m_\Sigma + m_\Xi) - \frac{x}{3}(m_\Sigma + m_\Xi - 2m_N) , \\
m_\Xi(x) &= \frac{1}{3}(m_N + m_\Sigma + m_\Xi) + \frac{x}{3}(2m_\Xi - m_N - m_\Sigma) , \\
m_\Sigma(x) &= \frac{1}{3}(m_N + m_\Sigma + m_\Xi) + \frac{x}{3}(2m_\Sigma - m_N - m_\Xi) , \\
m_\Lambda(x) &= \frac{1}{3}(m_N + m_\Sigma + m_\Xi) - \frac{x}{3}(m_\Sigma + m_N + m_\Xi - 3m_\Lambda) .
\end{aligned}$$

Masses without argument x denote the physical masses at $x = 1$. On this trajectory, the quantities

$$X_\pi^2 := \frac{1}{3} (2M_K^2(x) + M_\pi^2(x)) \quad \text{and} \quad X_N := \frac{1}{3} (m_N(x) + m_\Sigma(x) + m_\Xi(x))$$

stay constant, which corresponds (at next-to-leading order in BChPT) to a constant average quark mass. Moreover, the variation of $m_\Sigma(x) + m_\Lambda(x)$ is proportional to the famous Gell-Mann-Okubo difference,

$$\Delta_{\text{GMO}} := \frac{1}{4} (3m_\Lambda + m_\Sigma - 2m_N - 2m_\Xi) \approx 6 \text{ MeV} ,$$

and thus rather small, again in agreement with NLO BChPT. It has been nicely demonstrated in lattice QCD simulations that flavor-singlet related quantities like X_π^2 and X_N are remarkably constant when the flavor breaking is tuned while keeping the averaged quark mass fixed [57, 58]. At the same time, the flavor-breaking is described very well by terms linear in the quark-mass difference $m_s - \frac{1}{2}(m_u + m_d)$. We can thus be confident that our mass trajectories are in qualitative agreement with QCD.

In a similar manner, the meson decay constants should consistently be varied as

$$\begin{aligned} F_\pi(x) &= \frac{1}{3} (F_\pi + 2F_K) - \frac{2x}{3} (F_K - F_\pi) , \\ F_K(x) &= \frac{1}{3} (F_\pi + 2F_K) + \frac{x}{3} (F_K - F_\pi) , \\ F_\eta(x) &= \frac{1}{3} (F_\pi + 2F_K) + \frac{x}{3} (3F_\eta - F_\pi - 2F_K) , \end{aligned}$$

compare Eqs. (16)-(20) in [63]. Finally, the inverse ranges are also varied linearly in x ,

$$\alpha_{jb}(x) = \alpha_0 + x (\alpha_{jb} - \alpha_0) .$$

As we have no data to determine α_0 , the common inverse range in the symmetric limit, we simply adopt a reasonable value close to the average of the fitted physical inverse ranges, $\alpha_0 = 750 \text{ MeV}$, in analogy to the treatment of the subtraction constants in Sec. 3 and Appendix A of [11]. The sensitivity of our results to the selected α_0 value is discussed in Sec. 4.

References

- [1] Murray Gell-Mann. The Eightfold Way: A Theory of strong interaction symmetry. California Institute of Technology Synchrotron Laboratory Report No. CTSL-20, TID-12608, 1961.
- [2] Steven Weinberg. Phenomenological Lagrangians. *Physica*, A96(1-2):327–340, 1979.
- [3] J. Gasser and H. Leutwyler. Chiral Perturbation Theory: Expansions in the Mass of the Strange Quark. *Nucl. Phys.*, B250:465–516, 1985.
- [4] Elizabeth Ellen Jenkins and Aneesh V. Manohar. Baryon chiral perturbation theory using a heavy fermion Lagrangian. *Phys. Lett. B*, 255:558–562, 1991.
- [5] A. Krause. Baryon Matrix Elements of the Vector Current in Chiral Perturbation Theory. *Helv. Phys. Acta*, 63:3–70, 1990.
- [6] V. Bernard, Norbert Kaiser, and Ulf-G. Meißner. Chiral dynamics in nucleons and nuclei. *Int. J. Mod. Phys. E*, 4:193–346, 1995.
- [7] N. Kaiser, P. B. Siegel, and W. Weise. Chiral dynamics and the low-energy kaon-nucleon interaction. *Nucl. Phys.*, A594:325–345, 1995.
- [8] E. Oset and A. Ramos. Nonperturbative chiral approach to s wave $\bar{K}N$ interactions. *Nucl. Phys.*, A635:99–120, 1998.
- [9] J. A. Oller and Ulf-G. Meißner. Chiral dynamics in the presence of bound states: Kaon nucleon interactions revisited. *Phys. Lett.*, B500:263–272, 2001.
- [10] E. Oset, A. Ramos, and C. Bennhold. Low lying $S = -1$ excited baryons and chiral symmetry. *Phys. Lett. B*, 527:99–105, 2002. [Erratum: *Phys.Lett.B* 530, 260–260 (2002)].
- [11] D. Jido, J. A. Oller, E. Oset, A. Ramos, and Ulf-G. Meißner. Chiral dynamics of the two $\Lambda(1405)$ states. *Nucl. Phys.*, A725:181–200, 2003.
- [12] G. Beer et al. Measurement of the kaonic hydrogen X-ray spectrum. *Phys. Rev. Lett.*, 94:212302, 2005.

- [13] M. Bazzi et al. A New Measurement of Kaonic Hydrogen X-rays. *Phys. Lett.*, B704:113–117, 2011.
- [14] Yoichi Ikeda, Tetsuo Hyodo, and Wolfram Weise. Chiral SU(3) theory of antikaon-nucleon interactions with improved threshold constraints. *Nucl. Phys.*, A881:98–114, 2012.
- [15] Maxim Mai and Ulf-G. Meißner. New insights into antikaon-nucleon scattering and the structure of the $\Lambda(1405)$. *Nucl. Phys.*, A900:51 – 64, 2013.
- [16] A. Cieplý and J. Smejkal. Chirally motivated $\bar{K}N$ amplitudes for in-medium applications. *Nucl. Phys. A*, 881:115–126, 2012.
- [17] Zhi-Hui Guo and J. A. Oller. Meson-baryon reactions with strangeness -1 within a chiral framework. *Phys. Rev.*, C87(3):035202, 2013.
- [18] Albert Feijoo, Volodymyr Magas, and Angels Ramos. $S = -1$ meson-baryon interaction and the role of isospin filtering processes. *Phys. Rev.*, C99(3):035211, 2019.
- [19] Albert Feijoo, Daniel Gazda, Volodymyr Magas, and Angels Ramos. The $\bar{K}N$ interaction in higher partial waves. arXiv:2107.10560[hep-ph], 2021.
- [20] P. C. Bruns and A. Cieplý. Coupled channels approach to ηN and $\eta' N$ interactions. *Nucl. Phys. A*, 992:121630, 2019.
- [21] B. Borasoy, R. Nißler, and W. Weise. Chiral dynamics of kaon-nucleon interactions, revisited. *Eur. Phys. J. A*, 25:79–96, 2005.
- [22] M. Csejthey-Barth et al. The interactions of low energy K^- mesons with protons. *Phys. Lett.*, 16:89–91, 1965.
- [23] M. Sakitt, T. B. Day, R. G. Glasser, N. Seeman, J. H. Friedman, W. E. Humphrey, and R. R. Ross. LOW-ENERGY K- MESON INTERACTIONS IN HYDROGEN. *Phys. Rev.*, 139:B719, 1965.
- [24] J. K. Kim. Low Energy $K^- p$ Interaction of the 1405 MeV Y^* Resonance as $\bar{K}N$ Bound State. *Phys. Rev. Lett.*, 14:29, 1965.

- [25] Terry S. Mast, Margaret Alston-Garnjost, Roger O. Bangerter, Angela S. Barbaro-Galtieri, Frank T. Solmitz, and Robert D. Tripp. Elastic, Charge Exchange, and Total K^-p Cross-Sections in the Momentum Range 220-MeV/c to 470-MeV/c. *Phys. Rev.*, D14:13, 1976.
- [26] R. O. Bangerter, M. Alston-Garnjost, A. Barbaro-Galtieri, T. S. Mast, F. T. Solmitz, and R. D. Tripp. Reactions $K^-p \rightarrow \Sigma^- \pi^+$ and $K^-p \rightarrow \Sigma^+ \pi^-$ in the Momentum Range From 220-MeV/c to 470-MeV/c. *Phys. Rev.*, D23:1484, 1981.
- [27] J. Ciborowski et al. Kaon Scattering and Charged Sigma Hyperon Production in K^-p Interactions Below 300 MeV/c. *J. Phys.*, G8:13–32, 1982.
- [28] R. J. Nowak et al. Charged Sigma Hyperon Production by K^- Meson Interactions at Rest. *Nucl. Phys.*, B139:61–71, 1978.
- [29] D. N. Tovee et al. Some properties of the charged sigma hyperons. *Nucl. Phys.*, B33:493–504, 1971.
- [30] D. F. Baxter et al. A study of neutral final states in K^-p interactions in the range from 690 to 934 MeV/c. *Nucl. Phys. B*, 67:125–156, 1973.
- [31] M. D. Jones. A study of the reaction $K^-p \rightarrow \Sigma^0 \eta$ near threshold. *Nucl. Phys. B*, 73:141–165, 1974.
- [32] A. Starostin et al. Measurement of $K^-p \rightarrow \eta \Lambda$ near threshold. *Phys. Rev. C*, 64:055205, 2001.
- [33] Jonathan L. Rosner, Sheldon Stone, and Ruth S. Van de Water. Leptonic Decays of Charged Pseudoscalar Mesons. *Phys. Rev.*, D98(3):030700, 2018.
- [34] S. Aoki et al. FLAG Review 2019. *arXiv:1902.08191 [hep-lat]*, 2019.
- [35] Philip G. Ratcliffe. SU(3) breaking in hyperon beta decays: A Prediction for $\Xi^0 \rightarrow \Sigma^+ e \bar{\nu}$. *Phys. Rev.*, D59:014038, 1999.
- [36] Tetsuo Hyodo and Daisuke Jido. The nature of the $\Lambda(1405)$ resonance in chiral dynamics. *Prog. Part. Nucl. Phys.*, 67:55–98, 2012.

- [37] P. C. Bruns and A. Cieplý. Importance of chiral constraints for the pole content of the $\bar{K}N$ scattering amplitude. *Nucl. Phys. A*, 996:121702, 2020.
- [38] Ulf-G. Meißner. Two-pole structures in QCD: Facts, not fantasy! *Symmetry*, 12(6):981, 2020.
- [39] Maxim Mai. Review of the $\Lambda(1405)$. A curious case of a strangeness resonance. *Eur. Phys. J. ST*, 230(6):1593–1607, 2021.
- [40] Yong-seok Oh and Hung-chong Kim. Pentaquark baryons in SU(3) quark model. *Phys. Rev. D*, 70:094022, 2004.
- [41] V. Baru, J. Haidenbauer, C. Hanhart, Yu. Kalashnikova, and Alexander Evgenyevich Kudryavtsev. Evidence that the $a_0(980)$ and $f_0(980)$ are not elementary particles. *Phys. Lett. B*, 586:53–61, 2004.
- [42] D. Gamermann, J. Nieves, E. Oset, and E. Ruiz Arriola. Couplings in coupled channels versus wave functions: application to the X(3872) resonance. *Phys. Rev. D*, 81:014029, 2010.
- [43] F. Aceti and E. Oset. Wave functions of composite hadron states and relationship to couplings of scattering amplitudes for general partial waves. *Phys. Rev. D*, 86:014012, 2012.
- [44] Takayasu Sekihara, Tetsuo Hyodo, and Daisuke Jido. Comprehensive analysis of the wave function of a hadronic resonance and its compositeness. *PTEP*, 2015:063D04, 2015.
- [45] R. J. Eden and J. R. Taylor. Poles and Shadow Poles in the Many-Channel S Matrix. *Phys. Rev.*, 133:B1575–B1580, 1964.
- [46] B. C. Pearce and B. F. Gibson. Observable Effects of Poles and Shadow Poles in Coupled Channel Systems. *Phys. Rev.*, C40:902–911, 1989.
- [47] A. Cieplý, M. Mai, Ulf-G. Meißner, and J. Smejkal. On the pole content of coupled channels chiral approaches used for the $\bar{K}N$ system. *Nucl. Phys.*, A954:17–40, 2016.
- [48] Maxim Mai and Ulf-G. Meißner. Constraints on the chiral unitary $\bar{K}N$ amplitude from $\pi\Sigma K^+$ photoproduction data. *Eur. Phys. J.*, A51(3):30, 2015.

- [49] Hideko Nagahiro and Atsushi Hosaka. Elementarity of composite systems. *Phys. Rev. C*, 90(6):065201, 2014.
- [50] Zhi-Hui Guo and J. A. Oller. Probabilistic interpretation of compositeness relation for resonances. *Phys. Rev. D*, 93(9):096001, 2016.
- [51] Peter C. Bruns. Spatial interpretation of "compositeness" for finite-range potentials. *arXiv:1905.09196 [hep-ph]*, 5 2019.
- [52] R. Molina and M. Döring. Pole structure of the $\Lambda(1405)$ in a recent QCD simulation. *Phys. Rev. D*, 94(5):056010, 2016. [Addendum: *Phys.Rev.D* 94, 079901 (2016)].
- [53] Kenta Miyahara, Tetsuo Hyodo, and Wolfram Weise. Construction of a local $\bar{K}N - \pi\Sigma - \pi\Lambda$ potential and composition of the $\Lambda(1405)$. *Phys. Rev. C*, 98(2):025201, 2018.
- [54] Aaron Torok, Silas R. Beane, William Detmold, Thomas C. Luu, Kostas Orginos, Assumpta Parreno, Martin J. Savage, and Andre Walker-Loud. Meson-Baryon Scattering Lengths from Mixed-Action Lattice QCD. *Phys. Rev. D*, 81:074506, 2010.
- [55] Michael Lage, Ulf-G. Meißner, and Akaki Rusetsky. A Method to measure the antikaon-nucleon scattering length in lattice QCD. *Phys. Lett. B*, 681:439–443, 2009.
- [56] William Detmold and Amy Nicholson. Low energy scattering phase shifts for meson-baryon systems. *Phys. Rev. D*, 93(11):114511, 2016.
- [57] W. Bietenholz et al. Flavour blindness and patterns of flavour symmetry breaking in lattice simulations of up, down and strange quarks. *Phys. Rev. D*, 84:054509, 2011.
- [58] J. M. Bickerton, R. Horsley, Y. Nakamura, H. Perlt, D. Pleiter, P. E. L. Rakow, G. Schierholz, H. Stüben, R. D. Young, and J. M. Zanotti. Patterns of flavor symmetry breaking in hadron matrix elements involving u , d , and s quarks. *Phys. Rev. D*, 100(11):114516, 2019.
- [59] C. Curceanu et al. Kaonic Deuterium Measurement with SIDDHARTA-2 on DAΦNE. *Acta Phys. Polon. B*, 51:251–257, 2020.

- [60] Moskov Amaryan et al. Strange Hadron Spectroscopy with Secondary KL Beam in Hall D. arXiv:2008.08215[nucl-ex], 2020.
- [61] A. Cieplý and J. Smejkal. Separable potential model for K- N interactions at low energies. *Eur. Phys. J. A*, 43:191–208, 2010.
- [62] A. V. Anisovich, A. V. Sarantsev, V. A. Nikonov, V. Burkert, R. A. Schumacher, U. Thoma, and E. Klempt. Hyperon III: $K^-p - \pi\Sigma$ coupled-channel dynamics in the $\Lambda(1405)$ mass region. *Eur. Phys. J. A*, 56(5):139, 2020.
- [63] Peter C. Bruns, Ludwig Greil, and Andreas Schäfer. Chiral extrapolation of baryon mass ratios. *Phys. Rev.*, D87(5):054021, 2013.